EFFECT OF SHAPE AND SIZE ON THE TRANSPORT OF PARTICLES OVER THE TURBULENT FREE SURFACE OF A NATURAL STREAM

A Thesis

Submitted to the Faculty of the

University of Minnesota

by

Henri Roland Sanness Salmon

in Partial Fulfillment of the Requirements for the Degree of

Master of Aerospace Engineering and Mechanics

Filippo Coletti

May 2021

ACKNOWLEDGEMENTS

I am grateful for the support of my advisor, Filippo Coletti, who's excitement for particle-laden flows is infectious. He has always granted me freedom to pursue topics that I am passionate about and challenges me to think for myself allowing me to become a more self-sufficient engineer. I have enjoyed the opportunity to attend many meetings, the majority being virtual during these times, discussing my work with other group members and always concluded with photos of Carlos and Julia to keep moral high.

I owe a huge thanks and gratitude to Lucia Baker, without whom this experimental data would not have been available to me. I was able to aid Lucia in the acquisition of the final particle measurements when I was first joining the group in September of 2019. However, credit is owed to her as she conducted the majority of the data collection on hot summer days, trapped in a tent which blocked the cool breeze of the Saint Anthony Falls. This data was then at my disposal for analysis. She was always available to me, being a helpful resource and provided me with the necessary image processing and particle tracking tools used by our group.

I would never had gotten to this point without the love and support of my family and friends. Many thanks to my parents, Gaëtan and Holly, for believing in me, having my best interests in mind and always talking to me about my studies even though the material at hand may of been incomprehensible to them at times. To Roland and Lucille, who aspired to help their grandchildren obtain a higher education and pursue their dreams. To Matthew, a good friend from undergrad, who was always available as an outlet to decompress on weekends and after long strenuous days of research. He has become practically family at this point as we weathered the storm of the pandemic together in Minneapolis while distant from family.

Finally, none of this research would have been possible without the funding recommendation of the Legislative-Citizen Commission on Minnesota Resources (LCCMR) to the Minnesota Legislature who grants the Environment and Natural Resources Trust Fund (ENRTF) which has purpose to provide a long-term, consistent, and stable source of funding for activities that protect, conserve, preserve and enhance Minnesota's "air, water, land, fish, wildlife and other natural resources" for the benefit of current citizens and future generations.

ABSTRACT

Here we investigate experimentally the motion of floating particles of different shape and size on the turbulent free surface of a field-scale meandering stream, using particle tracking velocimetry. Millimetre-sized spheres are used as tracers to obtain mean and fluctuating velocity fields of the flow surface. We focus on an approximately homogeneous region, where the single-point and two-point velocity statistics follow the classic phenomenology of three-dimensional turbulence. We then consider centimetre-sized discs and rods, much larger than the dissipative scales but much smaller than the integral scales of the turbulence. As finite-sized inertial particles, these exhibit similar velocities as the small tracers but weaker and less intermittent accelerations. Consequently, the motion of the larger particles along their trajectories is more time-correlated, and their diffusion coefficient is larger. This is confirmed by the mean square displacement of single particles and mean square separation between particle pairs, both of which grow faster in time compared to the tracers. The discs are also found to disperse faster than rods of the same size, pointing the important role of the objects' shape in the transport dynamics.

TABLE OF CONTENTS

LIST OF TABLES

LIST OF FIGURES

Chapter 1

Introduction

Plastics are the most prevalent type of marine debris found in our oceans and great lakes posing potential threats to human health and the environment. In the ocean this debris is known to accumulate and forms garbage patches, the largest being the Great Pacific Garbage Patch located halfway between Hawaii and California (Lebreton et al. 2018). The International Union for Conservation of Nature estimates that at least 8 million tons of plastic end up in our oceans every year and make up 80% of all marine debris from surface waters to deep-sea sediments. Plastics vary in shape and size but ultimately degrade into very small pieces (so-called microplastics) that irreversibly pollute the environment. Recent findings demonstrate that about 1,000 rivers account for 80% of the global annual emissions of 0.8 to 2.7 million tons of plastics into the ocean per year, with small urban rivers among the most polluting (Meijer et al., 2021). Not only do rivers play a key role in transporting plastic waste to the world's oceans, but the riverine ecosystems themselves are affected by such pollution (van Emmerik & Schwarz, 2019). Hence, microplastics are becoming and most likely are already a part of our ecosystem, being ingested by wildlife and making their way into our bodies which is toxic. Several chemicals in the production of plastic materials are known to be carcinogenic and interfere with the body's endocrine system, causing developmental, reproductive, neurological, and immune disorders in both humans and wildlife (Barboza et al., 2018; Halden, 2010). Therefore, understanding how floating particles of various shapes and sizes are transported in natural streams is critical to reach a predictive understanding of how, when and where they can be captured before eventually degrading into microplastics. One of the crucial questions, which we begin to address in this thesis, is the rate at which floating particles of different shape and size spread over the surface of turbulent streaming waters.

Plastics are composed of bulk material whose density resembles that of freshwater and sea water. Thus, they often float, and their motion is influenced by flow features at the free surface. These flow features are often a result from turbulence at the air-water interface (free surface). Turbulence is incredibly complex and highly chaotic, involving a range of length and time scales. It is most common in turbulence research to consider a statistical description where the scaling behaviour of averaged quantities are studied. However, most studies on free surface turbulence have mainly focused on the topological features of the flow, often in relation to air-water gas fluxes (Shen & Yue, 2001; McKenna & McGillis, 2004; Turney & Benerjee, 2013; Herlina & Wissink, 2014), with only few studies concerned with the transport of particles. Particularly, Cressman et al. (2004), Bandi et al. (2007), and Lovecchio et al. (2013) found that tracer particles floating on the free surface of a turbulent liquid gather and cluster into string-like structures with a long lifetime. The free surface transport of particles with different shapes and sizes has only recently attracted interest. Parsa et al. (2011) investigated the rotation and alignment of elongated particles in two-dimensional (2D) turbulence, showing that the rods' major axis tends to preferentially align with the past stretching direction. The experiments by Xia et al. (2019) in wave-driven 2D turbulence considered the diffusion of neutrally buoyant floating discs and found that the diffusion coefficient increases as the ratio between the disc radius and the forcing

scale decreases. Again, in wave-driven 2D turbulence, Yang et al. (2019) investigated the diffusion of floating ellipsoids and found them to diffuse faster along their major axis when this is larger than the forcing scale. However, it should be noted that 2D turbulence crucially differs from free surface turbulence, in which vortex stretching is allowed along the direction normal to the surface (Shen et al., 1999).

A large amount of plastics are in our oceans and their concentrations at the surface depend on local conditions like wind and breaking waves. Large-eddy simulations of buoyant particles at the ocean surface have been conducted to show how microplastics can redistribute due to these turbulent mixing processes (Kukulka et al., 2012; Brunner et al., 2015), while others investigate the transport of plastics under waves (Isobe et al., 2014; DiBenedetto et al., 2017) due to Stokes drift. These studies provide valuable insight on how particles disperse throughout the ocean mixing layer however, as mentioned previously, a significant fraction of plastics float and studies characterizing their motion on the free surface are lacking.

Additionally, the controllability aspect of experiments in laboratories and numerical simulations are generally not attainable in nature, and thus needs to be addressed. Several field studies have been concerned with natural free surface flows, focusing on the effectiveness of free surface velocity measurements, e.g. for discharge estimation as well as flow monitoring during flood events. These include large-scale particle image velocimetry (LSPIV), acoustic Doppler velocimetry (ADV) and particle tracking velocimetry (PTV) (Jin & Liao, 2019; Tauro et al., 2016, 2019). The imaging techniques (LSPIV and PTV) have gained favour in recent years however, uneven natural illumination and lack of trackable floating objects on the free surface may severely affect the effectiveness of such methods.

To our knowledge, it is clear from the above, that there have been very few field studies that have investigated the transport of particles of different shape and size on the free surface characterizing their dispersion properties. Here we investigate experimentally the motion of floating particles on the turbulent free surface of a field-scale meandering stream. Applying PTV to millimetre-sized floating spheres (assumed as flow tracers), we obtain surface velocity fields which allow us to define an approximate homogeneous region of the free surface flow. Within that, we characterize the scales of the flow using the framework of classic turbulence theory. We then characterize the Lagrangian transport of the centimeter-sized floating discs and rods, and directly compare them to the behaviour of the tracers, highlighting the influence of shape and size on their velocity, acceleration and dispersion.

The organization of this thesis is as follows. In Chapter 2, we present a brief overview of fluid dynamics and homogeneous isotropic turbulence. In Chapter 3, we present the research facility, the different particles used to investigate the effect of shape and size and the imaging setup. We also provide a brief description of the image processing and particle tracking techniques employed to obtain particle trajectories. Chapter 4 begins by discussing the velocity fields and single-point statistics of the tracers which allows us to utilize Kolmogorov (1941) classic turbulence theory to define the spatial and temporal scales of the free surface turbulence. We then compare the larger particles to the tracers and characterise their

Lagrangian transport to investigate the influence of particle shape and size on their velocity, acceleration, and dispersion. To conclude this chapter we take a cursory glance at the orientation of the rods. Finally, in Chapter 6, we summarize the results presented in this thesis, and discuss future experiments that could compliment and extend the conclusions of this work.

Chapter 2

Theory

2.1 Governing Equations of Fluid Dynamics

In fluid dynamics there are two perspectives in which one can observes the rate at which fluid quantities change within a time dependant control volume $\mathcal{V}(t)$. In the Eulerian perspective, fluid properties are described at a fixed location in space. Whereas, in the Lagrangian perspective, properties of a fluid element are tacked in time as it moves through space. These two descriptions must be equal at the same point in time and are related by the operator known as the material derivative. The material derivative $\mathrm{D}/\mathrm{D}t$ measures the rate of change of a quantity, $\mathcal{F}(\mathbf{x}, t)$, following a fluid element and is given by:

$$\frac{\mathrm{D}}{\mathrm{D}t} = \frac{\partial}{\partial t} + \mathbf{u} \cdot \nabla \tag{1}$$

In other words, the total rate of change of $\mathcal{F}(\mathbf{x}, t)$ is equal to the rate of change of $\mathcal{F}(t)$ inside the fluid element plus any advection of that same quantity in and out of $\mathcal{V}(t)$. However, control surfaces and volumes are not fixed. In fact they deform continuously under the action of applied stress' (surface forces per unit area). To derive the conservation laws for fluids we make use of the Reynolds Transport Theorem which states:

$$\frac{\mathrm{D}}{\mathrm{D}t} \int_{\mathcal{V}(t)} \mathcal{F} \mathrm{d}\mathcal{V} = \int_{\mathcal{V}(t)} \left(\frac{\partial \mathcal{F}}{\partial t} + \nabla \cdot (\mathbf{u}\mathcal{F}) \right) \mathrm{d}\mathcal{V} \tag{2}$$

Applying this theorem to the conservation of mass, $\mathcal{F} = \rho$ the density, this gives us the rate of change of the total mass in the control volume, which must be zero if mass is conserved. Therefore, in vector notation, we have:

$$\frac{\partial \rho}{\partial t} + \nabla \cdot \rho \mathbf{u} = 0 \tag{3}$$

which is also referred to as the continuity equation. If the density of the fluid is constant in time and throughout space, the above reduces to:

$$\nabla \cdot \mathbf{u} = 0 \tag{4}$$

defining an incompressible fluid.

Similarly, using Newton's second law, $\mathbf{F} = m\mathbf{a}$, one can define the equation of motion for an incompressible fluid. Letting $\mathcal{F} = \rho\mathbf{u}$ the momentum density, and using Equation 2 which must equal the forces acting on the fluid one obtains:

$$\int_{\mathcal{V}(t)} \left(\frac{\partial \rho u_i}{\partial t} + \frac{\partial u_j \rho u_i}{\partial x_j} \right) \mathrm{d}\mathcal{V} = \int_{\mathcal{S}(t)} n_j \tau_{ji} \mathrm{d}\mathcal{S} + \int_{\mathcal{V}(t)} \rho g_i \mathrm{d}\mathcal{V} \tag{5}$$

The index notation i and j denote the vector components along each Cartesian axis (x, y, z). The first and second terms on the right hand side represent the surface and body forces acting on $\mathcal{V}$ respectively. Here g_i is the gravitational acceleration, $\mathcal{S}(t)$ is a control surface, n_j is a unit vector normal to that surface and τ_{ji} is the stress tensor. Using the Divergence theorem which relates the flux of a quantity through a surface to the volume integral of the divergence of that quantity the surface force term becomes:

$$\int_{\mathcal{S}(t)} n_j \tau_{ji} \mathrm{d}\mathcal{S} = \int_{\mathcal{V}(t)} \frac{\partial \tau_{ji}}{\partial x_j} d\mathcal{V} \tag{6}$$

For a Newtonian fluid τ_{ji} is given by:

$$\tau_{ji} = \tau_{ij} = -p\delta_{ij} + \mu \left(\frac{\partial u_i}{\partial x_j} + \frac{\partial u_j}{\partial x_i} \right) \tag{7}$$

where p is the pressure and μ is the dynamic viscosity of the fluid. Putting these equations together one arrives at:

$$\frac{\partial u_i}{\partial t} + u_j \frac{\partial u_i}{\partial x_j} = -\frac{1}{\rho} \frac{\partial p}{\partial x_i} + \nu \frac{\partial^2 u_i}{\partial^2 x_j} + g_i \tag{8}$$

where $\nu = \mu/\rho$ is the kinematic viscosity of the fluid. Together Equation 4 and 8 are famously know as the Navier-Stokes equations which governs the flow of an incompressible Newtonian fluid.

2.2 Homogeneous Isotropic Turbulence

All flows become unstable above a certain Reynolds number. The Reynolds number Re is a dimensionless quantity that represents the ratio of inertial forces to viscous forces and is defined as:

$$\mathrm{Re} = \mathcal{U}\mathcal{L}/\nu \tag{9}$$

where $\mathcal{U}$ and $\mathcal{L}$ are suitable velocity and length scales of the flow respectively. Nondimensionalization of the Navier-Stokes equations, neglecting body forces, one obtains the following:

$$\nabla^* \cdot \mathbf{u}^* = 0 \tag{10}$$

$$\frac{\partial \mathbf{u}^*}{\partial t^*} + \mathbf{u}^* \cdot \nabla^* \mathbf{u}^* = -\nabla^* p^* + \frac{1}{\mathrm{Re}} \nabla^{*2} \mathbf{u}^* \tag{11}$$

where the asterisk represents dimensionless quantities; i.e. $\mathbf{u}^* = \mathbf{u}/\mathcal{U}$, $\mathbf{x}^* = \mathbf{x}/\mathcal{L}$, $t^* = t/(\mathcal{L}/\mathbf{U})$ and $p^* = p/\rho\mathcal{U}^2$. As Re increases the nonlinear inertial term, $\mathbf{u}^* \cdot \nabla^* \mathbf{u}^*$, in the momentum equation dominates which causes instabilities. These grow over time and the flow ultimately becomes turbulent. Turbulent flows are chaotic and unpredictable by nature. However, there are certain useful predictions that can be made based on a variety of physical arguments that can potentially reveal some universal features. Freely evolving turbulence: turbulent fluctuations being advected by a mean flow, represents turbulence in its simplest and purest form. Using Reynolds decomposition the flow velocity at any point in time $u_i(\mathbf{x}, t)$ can be decomposed into two components:

$$u_i = \overline{u_i} + u_i{}' \tag{12}$$

where $\overline{u_i}$ is the mean flow and $u_i{}'$ are the turbulent fluctuations which are irregular, chaotic and unpredictable. These velocity fluctuations result from a multitude of eddies (spinning flow structures), that have a wide range of spatial and temporal scales, interacting with one another. In 1922, Richardson famously proposed the following:

"Big whirls have little whirls that feed on their velocity, and little whirls have lesser whirls and so on to viscosity."

In other words, large eddies, which are unstable, eventually break down into smaller eddies. Their kinetic energy is passed down to these smaller eddies that stemmed from it. These smaller eddies undergo the same process giving rise to even smaller eddies which inherit the energy of their predecessors, and so on until viscosity can effectively dissipate the kinetic energy. Richardson proposed that the turbulent kinetic energy (TKE) is continually transferred from the larger eddies that break up into smaller eddies until they are destroyed by viscous dissipation. Therefore, the dissipation rate of TKE, ϵ: the transfer of energy from the large scales to the small scales of motion, which is approximately equal to the rate of destruction of energy at the small scales is of significant importance in turbulence.

In 1941, Kolmogorov incorporated these ideas and postulated a handful of hypothesis' that have remarkable consequences. Today these hypothesis' are simply referred to as K41 theory. The first begin, the hypothesis of local isotropy which states that the small-scale turbulent motions are statistically homogeneous and isotropic. Therefore, even though the velocity fluctuations may appear to be quite random and different from one realization to the next, their statistical properties are reproducible. To compute ϵ we can consider the Eulerian second-order velocity structure function defined as the ensemble average of the

second moment of the Eulerian velocity difference, $\delta^E \mathbf{u}(\mathbf{r}) = \mathbf{u}(\mathbf{r}) - \mathbf{u}(\mathbf{x}+\mathbf{r})$, evaluated at points separated by a distance $\mathbf{r}$:

$$S_2^E(\mathbf{r}) = \langle \delta^E \mathbf{u}(\mathbf{r})^2 \rangle \tag{13}$$

Here angle brackets represent ensemble-averaging over all realizations. For homogeneous isotropic turbulence the scaling law for the second-order structure function is given by:

$$S_2^E(\mathbf{r}) = C_2(\epsilon \mathbf{r})^{\frac{2}{3}} \tag{14}$$

where the constant C2 is taken to be 2.0 (Saddoughi & Veeravalli, 1994; Pope, 2001). Continuing with K41 theory, namely, the first similarity hypothesis which states that for homogeneous isotropic turbulence the statistics of the small-scale turbulence depends only on two parameters: the kinematic viscosity ν and ϵ. One can then estimate the smallest dissipative scales of the turbulence using the following:

$$\eta = \left(\frac{\nu^3}{\epsilon}\right)^{\frac{1}{4}} \tag{15}$$

$$\tau_\eta = \left(\frac{\nu}{\epsilon}\right)^{\frac{1}{2}} \tag{16}$$

where η and τ_η are the Kolmogorov length and time scales respectively. To determine the largest turbulent scales of motion one can make use of the Eulerian velocity autocorrelation function:

$$\rho_i^E(\mathbf{r}) = \frac{\langle u_i'(\mathbf{x}) u_i'(\mathbf{x}+\mathbf{r}) \rangle}{{\sigma_i}^2} \tag{17}$$

where ${\sigma_i}^2 = \langle u_i'(\mathbf{x})^2 \rangle$ is the velocity variance. This informs us about the degree to which, the velocity components at different points in space are correlated. The integral length scale L_L is then defined by the characteristic decay length of the Eulerian velocity autocorrelation function which is equivalent to:

$$L_L = \int_0^\infty \rho_i^E(\mathbf{r}) d\mathbf{r} \tag{18}$$

Although, in homogeneous turbulence Equation 17 is simply related to Equation 13 by the following expression:

$$\rho_i^E(\mathbf{r}) = \frac{\langle u_i'(\mathbf{x},t)u_i'(\mathbf{x}+\mathbf{r},t)\rangle}{{\sigma_i}^2} = 1 - \frac{S_2^E(\mathbf{r})}{2{\sigma_i}^2} \tag{19}$$

Therefore in the Eulerian frame of reference one can calculate the velocity autocorrelation function using the second-order velocity sturcture function and vice versa.

2.3 Single-particle and Pair-particle Dispersion

To characterize the spreading rate of the floating particles, we consider two Lagrangian observables: single-particle and particle-pair dispersion. The former, known as Taylor's problem, examines how far, on average, a single particle will migrate from its point of origin in time. Following the classic framework of Taylor (1921), the single-particle diffusivity and mean square displacement (MSD) can be derived from the Lagrangian velocity autocorrelation function defined as:

$$\rho_i^L(\tau) = \frac{\langle \overline{u_i'(\mathbf{x}(t))u_i'(\mathbf{x}(t+\tau))}\rangle}{{\sigma_i}^2} \tag{20}$$

where overbar represents trajectory-averaging and the angle brackets indicate the ensemble-averaging over all particle trajectories. The diffusion coefficient K and MSD can be obtained by integrating the Lagrangian velocity autocorrelation once and twice respectively:

$$K = \frac{1}{2}\frac{\mathrm{d}X^2}{\mathrm{d}t} = {\sigma_i}^2 \int_0^t \rho_i^L(\tau)d\tau \tag{21}$$

$$X(t)^2 = 2{\sigma_i}^2 \int_0^t \int_0^{t'} \rho_i^L(\tau)d\tau dt' \tag{22}$$

Equivalently to Equation 22 one can directly compute the MSD of single particles using their trajectories:

$$\langle X(t)^2\rangle = \langle [\mathbf{x}(t) - \mathbf{x}(t_0)]^2\rangle \tag{23}$$

where $\mathbf{x}(t)$ is the position of the particle at time t and $\mathbf{x}(t_0)$ is the reference position at the origin of the trajectory (at time $t = 0$ s). Similar to a random walk process Taylor showed that the MSD of a particle in a turbulent flow initially increases with the square of time t^2 and subsequently as t. The change in scaling indicates the transition between the ballistic and diffusive transport regimes respectively.

The latter, known as Richardson's problem, considers on average, how rapidly a pair of particles will separate from each other. The relative dispersion between a pair of particles or mean square separation (MSS) is given by:

$$D^2(t) = \langle [\mathbf{x}_i(t) - \mathbf{x}_j(t)]^2 \rangle \tag{24}$$

where $x_i(t)$ and $x_j(t)$ are the positions of the i-th and j-th particles at time t respectively and the angle brackets represent averaging over all i-j particle pairs. Batchelor (1950) refined Richardson's theory applying K41 and predicted that the MSS should grow ballistically for short times and that the initial separation $D_0 = D(t_0)$ should enter the scaling law. For longer times we expect the MSS to follow Richardson (1926) prediction of t^3 which is given by the Richardson-Obukhov law:

$$\langle [D(t) - D_0]^2 \rangle = \begin{cases} \frac{11}{3} C_2 (\epsilon D_0)^{2/3} t^2 & \text{for} \quad t < t_0 \\ g \epsilon t^3 & \text{for} \quad t > t_0 \end{cases} \tag{25}$$

where $t_0 = (D_0^2/\epsilon)^{1/3}$ is the characteristic time scale of an eddy of size D_0 and g is termed the Richardson constant. There have been attempts to recover the Richardson-Obukhov scaling in experiments however no convincing evidence has been found and estimates of the Richardson constant span a full order of magnitude (Ouellette et al., 2006b; Berk & Coletti, 2021; Sawford, 2001).

Chapter 3

Experimental Methods

3.1 Stream Facility and Hydrodynamic Characterization

Measurements are performed at an outdoor field-scale meandering stream facility at the University of Minnesota Saint Anthony Falls Laboratory (Figure 1). The Outdoor StreamLab (OSL) is an experimental stream channel and floodplain that offers laboratory-quality measurements and control in a field-scale setting. The OSL provides measurable bathymetry, controllable flow rates and allows the ability to seed particles homogeneously onto the surface of the stream. Water is drawn from the Mississippi River, flows through the stream channel and discharges back into the river. The flow rate is controlled via a valve at the inlet, and the incoming water flows into a headbox and over a weir before entering the stream channel. The height of the water at the weir is measured using a Massa M300 ultrasonic distance probe which allows real-time calculation of the flow rate. In the present experiment two flow rates are considered, $Q = 32.1$ L/s and 53.7 L/s. At these relatively low flow rates, suspension and transport of sediment is negligible, and the bed is static. The region of interest (ROI) in which particle measurements are taken is in one of the meanders in the stream and shown in Figure 2a. Vegetation growing on the banks are trimmed away or pinned down so that the flow is unobstructed.

Figure 1: The OSL facility, with the location of the region of interest (ROI) indicated by an arrow. The tent, shown here at a downstream location, covers the ROI in the present experiment.

The bathymetry of the ROI is shown in Figure 2b. Here we choose our coordinate system such that x is approximately in the streamwise direction pointing downstream so that the flow is left to right, y is in the spanwise direction pointing from the inner bank to the outer bank so that the meander has a concave curvature, and z is pointing vertically upward so that the origin ($z = 0$ m) is located at the water surface. The hydrodynamic conditions of the flow within the ROI are summarized in Table 1. The Reynolds number $\mathrm{Re} = D_H U_{bulk}/\nu$ and the Froude number $\mathrm{Fr} = U_{bulk}/\sqrt{gD_h}$ are based on the hydraulic depth $D_H = A/W$

and bulk velocity $U_{bulk} = Q/A$, where $g = 9.81$ m/s^2 is the gravitational acceleration, $\nu = 1.004 \cdot 10^{-6}$ m^2/s is the kinematic viscosity of water, and W and A are the mean width and cross-sectional area of the channel, respectively. The Froude number is another dimensionless parameter which represents the ratio between inertial and gravitational forces. It is necessary when considering the effect of waves in water channels. The denominator represents the speed of a wave on the water surface relative to the speed of the water. As suggested by the subcritical Fr (Fr < 1) and confirmed by visual inspection, the free surface is not macroscopically disturbed except for the presence of small waves. Indeed, considering the length and velocity scales of the free surface turbulence described later and using the parameter space suggested by Brocchini & Peregrine (2001) we are in a condition (Region 0 in their paper) where little surface disturbance is expected. Examining instantaneous images of the free surface (acquired as described later), these surface waves are observed to have wavelengths of about 3 cm and 6 cm for the low and high flow rates respectively. The RMS wave amplitude, obtained from the ultrasonic distance probe measurements, is about 0.7 mm for the high flow rate. From this we estimate the Stokes drift velocity associated with the pure wave motion to be at least one order of magnitude smaller than the RMS velocity fluctuations measured by PTV. This confirms that we are in a regime where waves do not significantly alter the transport of fluid elements.

(a) (b)

Figure 2: (a) The ROI and (b) its bathymetry for the high flow rate, with the black circles indicating the acoustic Doppler velocimetry (ADV) measurement locations.

Table 1: Key hydrodynamic parameters of the ROI: volumetric flow rate Q, mean width of the channel W, mean spanwise cross-sectional area of the channel A, bulk fluid velocity U_{bulk}, hydraulic diameter D_H, Reynolds number Re, and Froude number Fr.

	Low flow	High flow
Q [L/s]	32.1	53.7
W [m]	1.733	1.733
A [m^2]	0.145	0.177
U_{bulk} [m/s]	0.221	0.304
D_H [m]	0.084	0.102
Re	18 450	30 870
Fr	0.244	0.304

The OSL is also equipped with a movable traverse spanning the channel width on which

a side-looking Nortek Vectrino acoustic Doppler velocimetry (ADV) probe is mounted to perform cross-section velocity measurements. Three-component subsurface velocity (u, v, w) and two-component surface velocity (u, v) measurements are collected at 100 Hz for 120 seconds at several points along the cross-section at $x = 1$ m. This traverse is used to obtain temporal mean velocity ($\overline{u_i}$) and root mean square (RMS) velocity fluctuations (σ_{u_i}). ADVs are prone to recording occasional spurious velocity spikes due to bubbles or water velocities outside of the range that the ADV is set up to measure. To remove these sporadic spikes, the velocity signals are filtered using the phase-space thresholding technique described in Parsheh et al. (2010). The cross-sectional ADV measurements of the streamwise component of water velocity ($\overline{u}$) at various depths are shown in Figure 3. The flow appears to be strongly turbulent throughout the depth, with RMS velocity fluctuations (σ_u) highest close to the channel bed, which is expected due to the shear present at the bed-water interface, but larger that about $0.1U_{bulk}$ at most other measurement locations. This suggests that the turbulent dynamics we will observe, on the surface, is largely the footprint of the sub-surface turbulence.

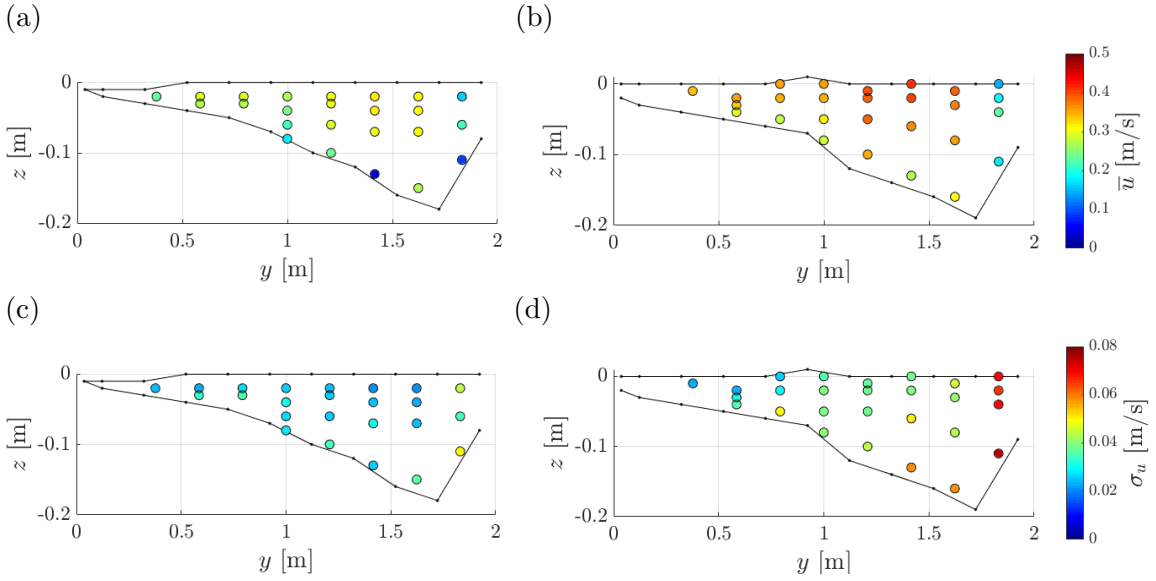

Figure 3: The mean (a,b) and RMS fluctuations (c,d) of the streamwise velocity measured by the AVD probe at various points in the cross-section for the low (a,c) and high (b,d) flow rate.

3.2 Floating Particles

Three types of floating particles are used in this study to investigate the effect of shape and size. White polypropylene bean-bag filler pellets, approximately spherical with a 5 mm diameter, are used to characterize the surface flow. The sphere were chosen as their properties satisfy multiple requirements which include:

I. Are sufficiently large to be accurately detected by imaging and recaptured downstream of the ROI so that we do not pollute the Mississippi River.

II. Have slight positive buoyancy such that they float.

III. Are sufficiently small to follow the free surface flow and can be accurately detected by imaging.

In Nikora et al. (2007), 3 mm floating particles were deemed suitable as tracers for free surface turbulence. In three-dimensional (3D) turbulence, neutrally buoyant particles 5 times larger than the Kolmogorov scale η are considered good flow tracers (Fiabane et al., 2012), and even for particle sizes of about 10η the response time was found to be only about 1.5 times that of fluid tracers (Qureshi et al. 2007; Volk et al., 2011). As it will be shown, the estimated Kolmogorov length scale of the free surface turbulence is about 12 times smaller than the sphere diameter; but the latter is about 35 to 50 times smaller than the energy-containing eddies. Therefore, while the spheres may not respond faithfully to the smallest fluctuations, they are expected to capture most of the turbulent fluctuations. To explore the effect of shape and size on particle transport, larger centimetre-sized discs and rods are considered. The discs consist of wooden craft circles and the rods are wooden toothpicks; mimicking the behaviour of rigid oblate and prolate ellipsoids respectively (Voth & Soldati, 2016). Both are spray-painted white to increase their visibility in images and to reduce their absorption of water. The different particle properties are summarized in Table 2.

Table 2: Summary of floating particle parameters including the material, density, major axis length, minor axis length and thickness.

Particle Type	Tracers	Discs	Rods
Material	Polypropylene	Wood	Wood
Density [g/cm^3]	0.9	0.7	0.7
Major Axis [mm]	5.0	38.1	63.5
Minor Axis [mm]	5.0	38.1	1.8
Thickness [mm]	N/A	3.2	N/A

3.3 Particle Imaging and Tracking

The imaging set up is shown in Figure 4. A 1-megapixel CMOS camera (Allied Vision Mako U-130B) with a 3-mm wide-angle lens is mounted on a cantilever arm attached to the traverse. The camera is suspended 60 cm downstream of the traverse and 1.5 m above the water surface, imaging a 2.2 m x 1.7 m field of view (FOV) below. To minimize reflections on the water surface due to direct sunlight, a large tent with side walls is set up to enclose the camera and the FOV. The tent also blocks any wind that may affect the free surface. To recapture the floating particles, a nylon seine net with 1.6 mm mesh is suspended from a PVC pipe frame across the channel 3 m downstream of the ROI. Particles are manually seeded into the channel surface by gently shaking them from a wide bin spanning the channel width upstream of the ROI. The camera records images at a frame rate of 30 Hz for the lower flow rate and 40 Hz for the higher flow rate. Four runs are performed for each case, resulting in 15,000 to 20,000 images, yielding approximately 16,000 particle trajectories for the tracers and 1,000 particle trajectories for the discs and rods, per each case. Multiple runs are performed to prevent the net from becoming filled with particles and blocking the water flow. Between each run, the particles are retrieved from the net, dried, and reused in succeeding runs.

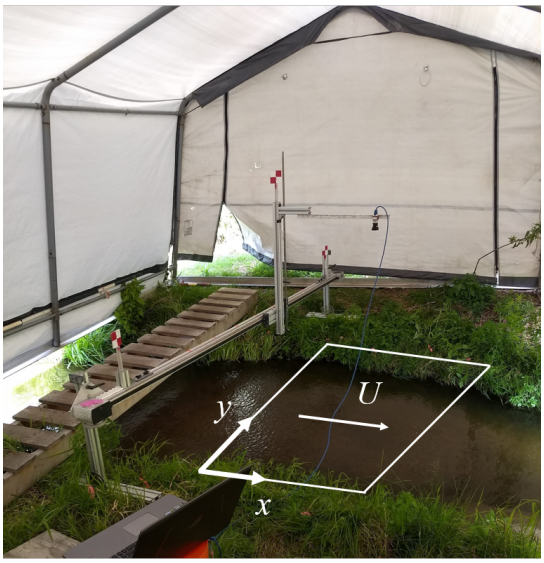

Figure 4: Photograph of the imaging setup, indicating the approximate location of the field of view (FOV), coordinate system and direction of the flow.

The wide-angle camera lens introduces image distortion. To correct them, a 0.9 m x 1.2 m checkerboard pattern is imaged and MATLAB's computer vision tools are used to determine the appropriate de-wrapping to correct the distortion. Furthermore, background noise must be removed from the images before preforming PTV. While the tent blocks direct sunlight, some glare off the water surface form the diffused ambient light is still present. These reflections vary in time due to the moving surface waves. The time-dependent background noise is removed using the proper orthogonal decomposition (POD)-based method described in Mendez et al. (2017); in this technique, images are decomposed into POD modes contributing to intensity variance. We subtract the first two modes, which successfully removes most of the glare and background noise while preserving the particle data (Figure 5).

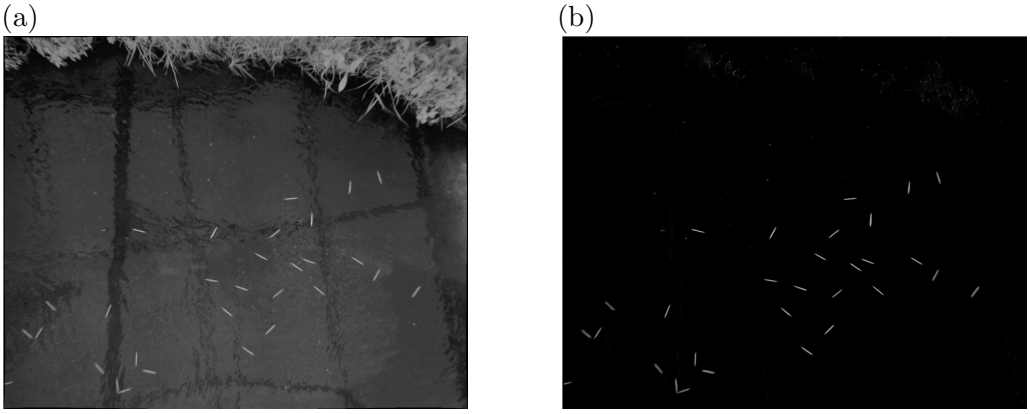

Figure 5: Example image of floating rods: (a) raw image and (b) background-subtracted image using the POD-based method.

Particles are detected by identifying contiguous groups of pixels exceeding an intensity threshold in the recorded images and checking the size of these objects against the expected size of the particle. We then consider the probability distribution function (PDF) of the areas of these groups of pixels that are detected and set a rejection criterion to be ± 2 standard deviations from the expected value (based on the pixel/mm ratio). This corresponds to a 95% confidence interval. Objects whose area does not lie within this interval are rejected and the remainder are counted as detected particles. Particle centroids of the detected particles are then found by calculating the centroids of the corresponding continuous groups of pixels in the images. These centroids are then tracked using a nearest neighbour PTV algorithm that minimizes particle acceleration (Ouellette et al. 2006a), and their velocities and accelerations are obtained from the trajectories by convolution with the derivative of a Gaussian kernel in the time domain, as described in Baker & Coletti (2020). The size of the temporal kernel t_k is chosen as the value beyond which the total acceleration variance $({\sigma_a}^2)$ decays exponentially, i.e. exhibits a power-law behaviour, as done in several previous studies (Voth et al., 2002; Nemes et al., 2017; Berk & Coletti, 2021) and shown in Figure 6a. The temporal kernel then defines the minimum length a trajectory must have for smoothing. A small subset of the recorded trajectories for the tracers is shown in Figure 6b for illustration.

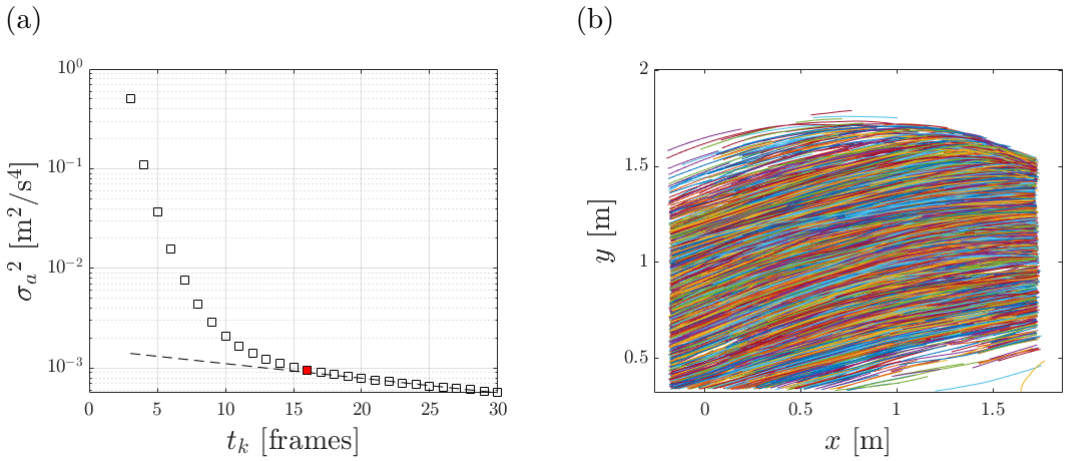

Figure 6: (a) Particle acceleration variance plotted against the Gaussian smoothing kernel size for the tracers in the low flow rate case. The data point highlighted in red corresponds to the chosen kernel size for this data set and the dashed line represents the exponential decay of the acceleration variance. (b) 1% of the corresponding smoothed particle tracks of the tracers for the low flow rate, drawn in different colours for visualization.

Chapter 4

Results and Discussion

4.1 Flow Characterization

We first characterize the properties of the free surface turbulence using the small tracer particles. To define Eulerian fields of U_{mean} (the mean of the norm of the velocity $U = \sqrt{u^2 + v^2}$) and RMS fluctuations (σ_U), the PTV trajectories are binned in fixed interrogation windows. The size of each window is approximately 25 cm^2, which permits that at least 25 samples are measured in each window over the entire data set. The results are shown in Figure 7, which also displays the corresponding near-surface ADV measurements made 2 cm below the water surface. These are in reasonable agreement with the Eulerian velocity fields obtained from PTV, except for a region near the shallow inner bank (Figure 7a). In order to perform a statistical analysis of the data, we define a 1.25 m x 1 m sub-region of the FOV where the flow is quasi-homogeneous: the mean flow velocity and the RMS fluctuations in it are within ± 2.5% and 9.3% of their respective spatial mean for the low flow rate, and ± 3.4% and 13.5% for the high flow rate case. In addition, the streamlines within this sub-region are relatively straight. The following presents results obtained over this sub-region.

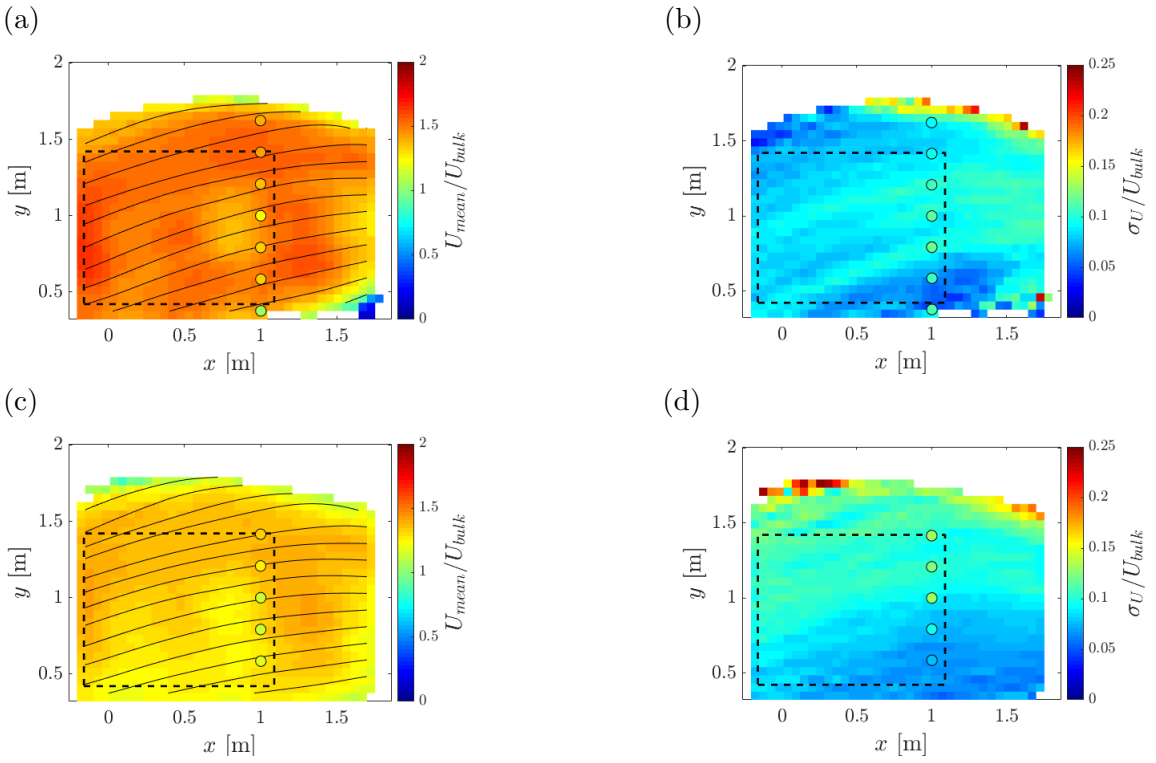

Figure 7: (a, c) Eulerian mean velocity and (b, d) RMS velocity fluctuation fields of the tracers for the low (a, b) and high (c, d) flow rate cases, normalized by U_{bulk}. The flow direction is left to right. The dashed box indicates the sub-region of the flow where approximate homogeneity and isotropy is observed, and the black lines indicate streamlines. The colored circles correspond near-surface ADV measurements respectively.

We first consider the single-point statistics of the tracers. Figure 8 displays the PDFs of the streamwise and spanwise velocity fluctuations for the low and high flow rates as well as the PDF of the streamwise and spanwise accelerations for both flow rates. The instantaneous velocity fluctuation vector $\mathbf{u}$ is calculated by subtracting from the measured velocity the mean velocity $\langle \mathbf{u} \rangle$. Here and in the following, angle brackets indicate ensemble-averaging over all realizations and all spatial locations within the homogeneous sub-region. One can clearly see the isotropy of the velocity fluctuations, with the PDFs closely approximating a Gaussian distribution (Figure 8a, 8c). On the other hand, the acceleration PDFs (which have approximately zero mean) possess long exponential tails, indicating strong intermittency, i.e. relatively strong probability of extreme events occurring, which increases with Re (Figure 8b, 8d). This behaviour has been well documented in 3D turbulence (Voth et al., 2002; Mordant et al., 2004). The measured kurtosis' are reported in Table 3 while the kurtosis of the velocity fluctuations equals the Gaussian value of 3. It should be noted that the small departure from Gaussianity for the left tails of the velocity PDFs (Figure 8a, 8c) is likely due to the imperfect homogeneity in the flow field near the shallow inner bank. Quantitatively equivalent results (for these and the following observables) are obtained if one defines a curvilinear coordinate system that follows the meander's curvature.

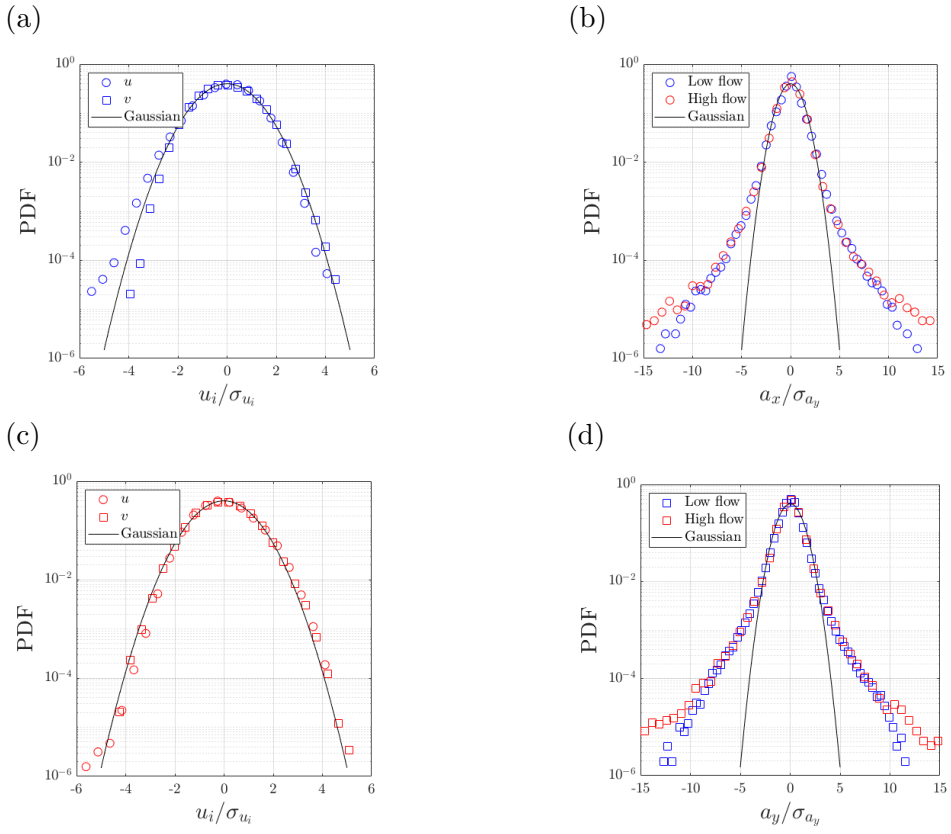

Figure 8: (a, c) PDFs of the streamwise and spanwise velocity fluctuations for the tracers in the low (a) and high (c) flow rates. PDFs of the (b) streamwise and (d) spanwise acceleration fluctuations for the low (blue) and high (red) flow rate cases. The distributions in each panel are normalized by their respective standard deviations. The continuous lines represent a normalized Gaussian distribution.

Table 3: Kurtosis' of the streamwise and spanwise acceleration PDFs for both flow rates.

	Low flow	High flow
κ_{a_x}	7.0	11.1
κ_{a_y}	8.1	15.9

Next, we consider the two-point statistics of the tracers, specifically the longitudinal Eulerian second-order structure function of the velocity fluctuations. Focusing on the longitudinal structure function in Equation 13, we consider the components of the velocity parallel to the separation vector $\mathbf{r}$ (Pope, 2001). Figure 9a shows that the structure function exhibits an approximate $r^{2/3}$ scaling over an intermediate range of scales (separations from about 3 cm to 10 cm). This suggests the use of Kolmogorov (1941) classic theory to determine the dissipation rate ϵ of the turbulent kinetic energy. While the applicability of Kolmogorov theory to free surface turbulence is debated (Hunt & Graham, 1978; Magnaudet, 2003), experimental and numerical studies have clearly shown the presence of a -5/3 slope of the energy spectra at or near the free surface (Chickadel et al., 2011; Flores et al., 2017), which is equivalent to the 2/3 scaling of the second-order structure function. Flores et al. (2017) report that, even though the mechanism underlying the spectral slope is different compared to 3D turbulence, the proportionality constants are roughly the same. Therefore, here we assume $C_2 = 2.0$ as in 3D turbulence and use Equation 14 to estimate ϵ. The value of the latter is found from the plateau of the compensated structure function in Figure 9b, which is plotted in units of $\mathrm{m}^2/\mathrm{s}^3$. Using these dissipation values, we can estimate the smallest (dissipative) scales of the free surface turbulence, i.e. the Kolmogorov length and time scale using Equation 15 and 16 respectively. To determine the integral length scales of the free surface turbulence we make use of the Eulerian velocity autocorrelation function calculated using Equation 19 (owing to the fact of the homogeneous sub-region considered), and is plotted in Figure 9c. As the Eulerian autocorrelation function exhibits an approximate exponential decay (a physical decay up to $r = 0.12$ m), the integral length scale L_L is evaluated by least-square fitting to it a function $A\mathrm{e}^{-r/L_L}$, where A is a constant. From the latter, an alternative estimate of the dissipation rate can be obtained from the scaling (Tennekes & Lumley, 1972):

$$\epsilon \approx C\frac{\langle\sigma_U\rangle^3}{L_L} \tag{26}$$

where the constant C is approximately 0.5 in high-Re 3D turbulence (Burattini et al. 2005; Carter et al., 2016). We find that these estimates are very close to those found from the compensated second-order structure function. The characteristics of the free surface turbulence are summarized in Table 4.

As mentioned above, the Kolmogorov scales η are one order of magnitude smaller than the sphere diameter, and approximately two order of magnitude smaller than the diameter (length) of the discs (rods). Therefore, it should be emphasized that the smallest particles used in these experiments are not perfect tracers and in consequence the scales reported are only approximate estimates. However, we anticipate the discs and rods to exhibit significant

finite-size effects. In addition, even they are much smaller than L_L, which represents the size of the energy-containing eddies, and thus they are expected to follow the large-scale motions of the free surface. The separation between the Kolmogorov and integral scales is consistent with the appearance of an inertial sub-range exhibiting the observed $r^{2/3}$ scaling of the Eulerian structure function (Pope, 2001). Nevertheless, the primary objective of this experiment was to investigate the transport properties of floating particles whose shape and size differs on the turbulent free surface of a natural stream as opposed to characterizing the free surface turbulence itself.

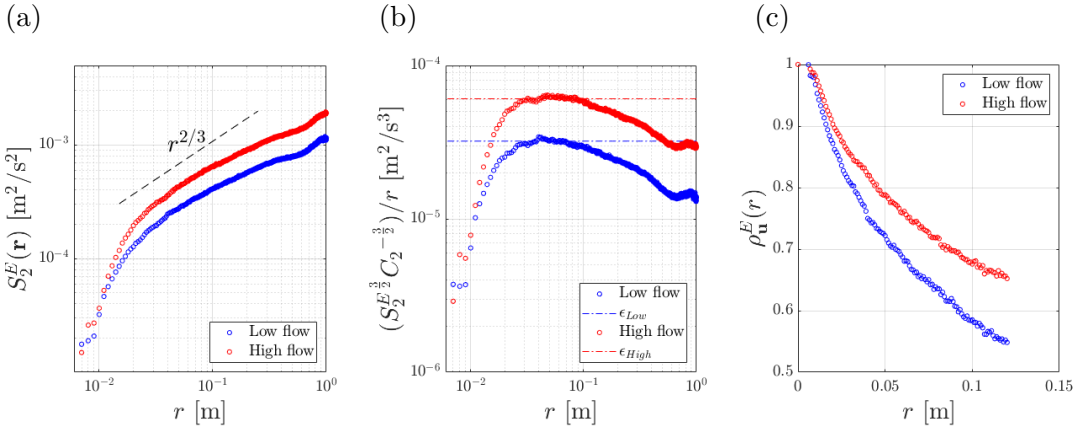

Figure 9: (a) Longitudinal Eulerian second-order velocity structure function, (b) compensated structure function and (c) Eulerian velocity autocorrelation function for the tracers in the low (blue) and high (red) flow rate. The dashed line in (a) corresponds to $r^{2/3}$ scaling. The dash-dotted horizontal lines in (b) show the plateau of the compensated structure function which corresponds to the turbulent dissipation rate.

Table 4: Main physical quantities characterizing the free surface turbulence for both flow rates: the RMS of velocity fluctuations $\langle\sigma_U\rangle$, integral length scale L_L, dissipation ϵ (using Equation 14 and 26), Kolmogorov length scale η, and the Kolmogorov time scale τ_η.

	Low flow	High flow
$\langle\sigma_U\rangle$ [m/s]	0.022	0.032
L_L [m]	0.175	0.243
ϵ from Equation 14 [m^2/s^3]	$3.2 \cdot 10^{-5}$	$6.1 \cdot 10^{-5}$
ϵ from Equation 26 [m^2/s^3]	$3.1 \cdot 10^{-5}$	$6.6 \cdot 10^{-5}$
η [mm]	0.4	0.4
τ_η [s]	0.18	0.13

4.2 Effect of Particle Shape and Size

In this section we compare the motion of the larger particles (discs and rods) against the tracers. First, we consider the mean velocity (Figure 10) and RMS velocity fluctuation (Figure 11) fields of all particle types and verify that they are quantitatively similar. This is evident by inspecting the mean velocity fields of the discs and rods at the low flow rate (Figure 10a, 10b) against the tracer velocity field in the same regime (Figure 7a). Quantitatively equivalent observations can be made comparing the RMS velocity fluctuations and

other flow rates. Table 5 reports the maximum and RMS differences between those fields for both discs and rods under both considered flow rates, calculated in the homogeneous sub-region. The differences are marginal when compared to U_{bulk}.

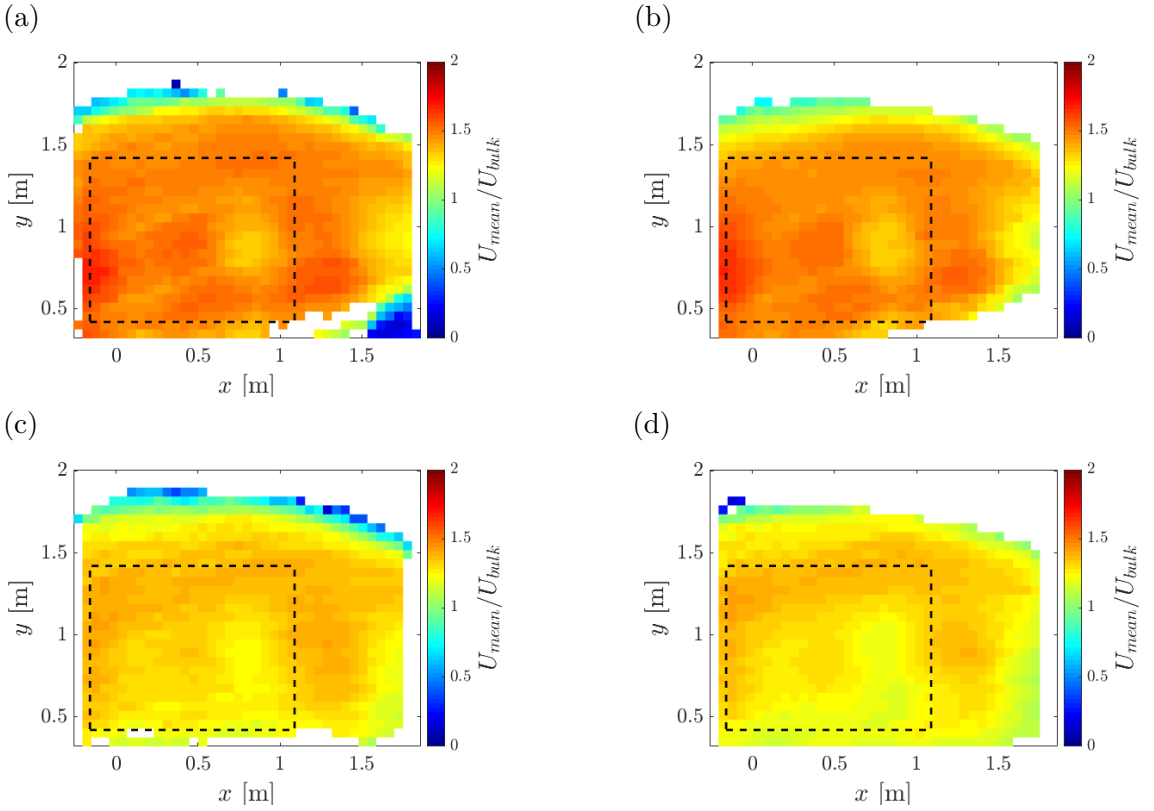

Figure 10: Mean velocity fields of the discs (a, c) and the rods (b, d) in the low (a, b) and high (c, d) flow rates. A comparison with the tracer velocity field (Figure 7a, 7c) indicates marginal differences. The dashed box indicates the sub-region of the flow where approximate homogeneity and isotropy is observed.

Table 5: Maximum and RMS absolute difference with respect to the tracer velocity fields for the discs and rods, in both considered flow rates, normalized by U_{bulk}.

	Discs (Low flow)	Rods (Low flow)	Discs (High flow)	Rods (High flow)
$\Delta U_{\mathrm{MAX}}/U_{bulk}$	0.04	0.02	0.005	0.005
$\Delta U_{RMS}/U_{bulk}$	0.003	0.001	0.004	0.001

The PDFs of the streamwise (Figure 12a, 13a) and spanwise (Figure 12b, 13b) velocity fluctuations are also similar between all particle types, closely approximating a Gaussian distribution. This is dictated by the large scales of the turbulence. On the other hand, the acceleration variance is significantly reduced for the larger particles (Figure 12c, 12d, 13c, 13d). The accelerations of all particles display some intermittency, but this is visibly attenuated for the larger particles. This indicates that the discs and rods filter out the higher acceleration events, which are associated to the smallest scales of the turbulence

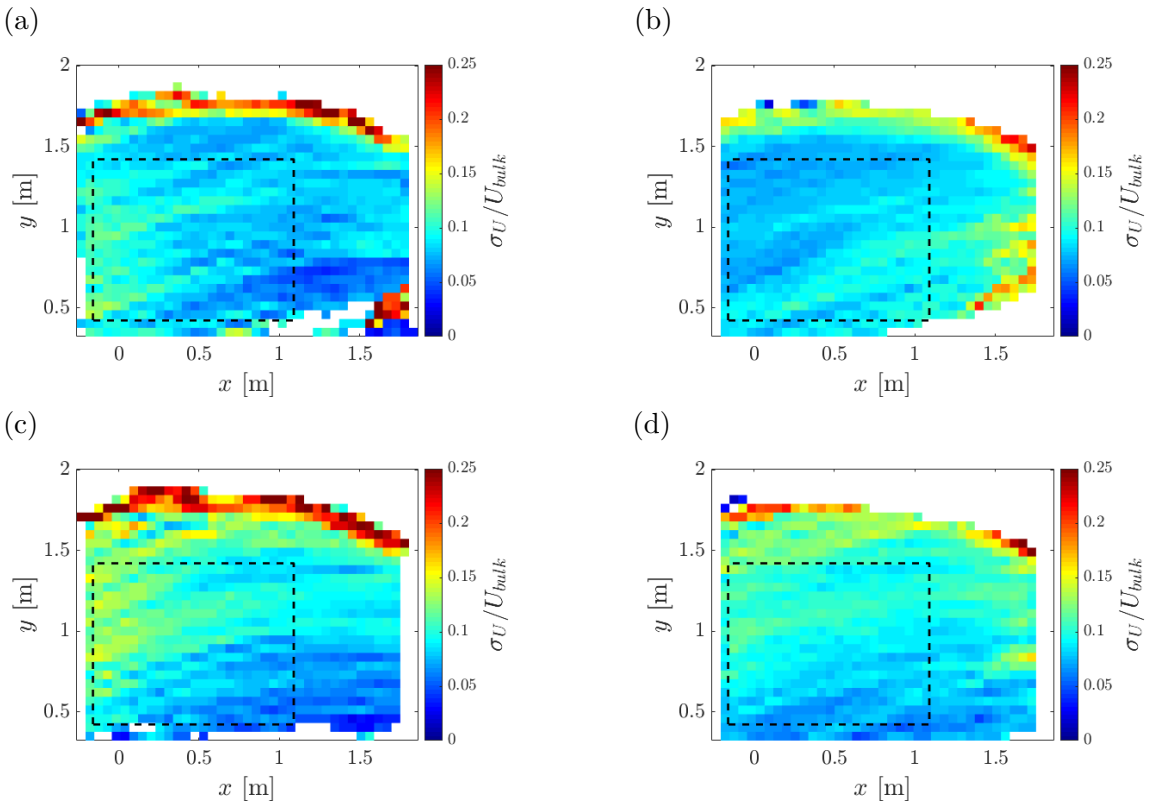

Figure 11: RMS velocity fluctuation fields of the discs (a, c) and the rods (b, d) at the low (a, b) and high (c, d) flow rate cases. A comparison with the tracer velocity field (Figure 7b, 7d) indicates marginal differences. The dashed box indicates the sub-region of the flow where approximate homogeneity and isotropy is observed.

(Sreenivasan & Antonia, 1997). Such a behaviour, known as inertial filtering, has long been identified by studies concerned with inertial particles in 3D turbulence (Voth et al., 2002; Toschi & Bodenschatz, 2009; Volk et al. 2011).

To characterize the spreading rate of the floating particles, we consider their Lagrangian motion: particularly single-particle and particle-pair dispersion. As mention previously, the former examines how far, on average, a single particle migrates from its origin over time. Leveraging the homogeneity of the flow in the considered sub-region and following the classic framework of Taylor (1921), the single-particle diffusivity coefficient can be derived from the Lagrangian velocity autocorrelation:

$$\rho_U^L(\tau) = \left\langle \frac{\overline{U(\mathbf{x}(t))U(\mathbf{x}(t+\tau))}}{\overline{U(\mathbf{x}(t))^2}} \right\rangle \tag{27}$$

As compared to Equation 20, the above is computed using the instantaneous velocity fluctuation U; calculated by subtracting from the measured norm of the velocity its mean $\langle U \rangle$. Here the overbar represents trajectory-averaging; it is associated with the number

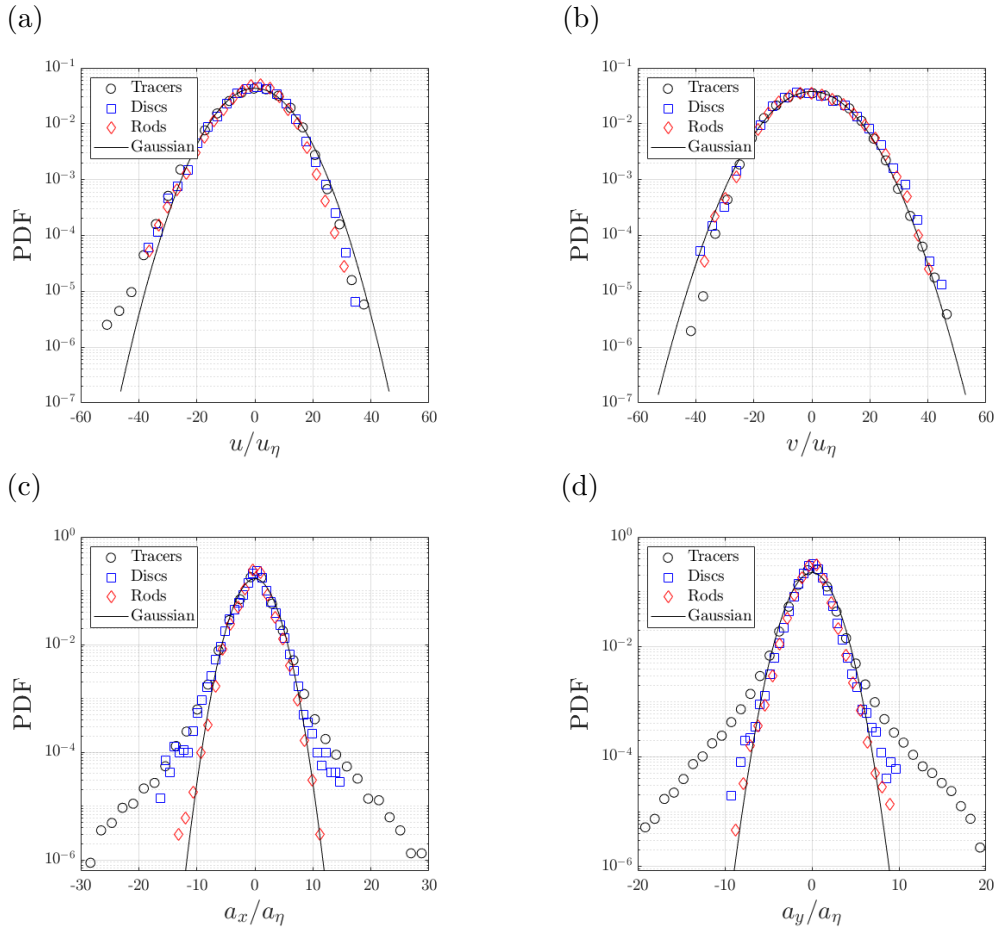

Figure 12: PDFs of the streamwise (a, c) and spanwise (b, d) velocity fluctuations (a, b) and accelerations (c, d) for the different particle types in the low flow rate. The distributions are normalized by Kolmogorov scaling. The continuous lines represent normalized Gaussian distributions.

of linked points (in time) forming each trajectory. The autocorrelation is first calculated along each trajectory and normalized by its velocity variance, before ensemble-averaging over all trajectories. This procedure ensures that each trajectory has the same weight when contributing to the global autocorrelation coefficient regardless of its variance (Guala et al., 2007). Additionally, we only consider the velocity variance of trajectories whose duration is longer than the time delay τ (Mordant et al., 2004). These tracks are the only ones to contribute to the estimation of $\rho_i^L(\tau)$ as obviously $u_i'(t)$ and $u_i'(t+\tau)$ cannot be measured for tracks shorter than τ. Figure 14 displays the Lagrangian velocity autocorrelation of each particle type for both considered flow rates. Seemingly, the motion of the discs and rods is more time-correlated than that of the tracers. This is consistent with our previous findings that the larger particles filter out the small-scale turbulent motions. In fact, this agrees with the trend found in numerical simulations of small inertial particles (Squires & Eaton, 1991; Jung et al., 2008) and laboratory observations of finite-size particles (Machicoane & Volk, 2016) in 3D turbulence.

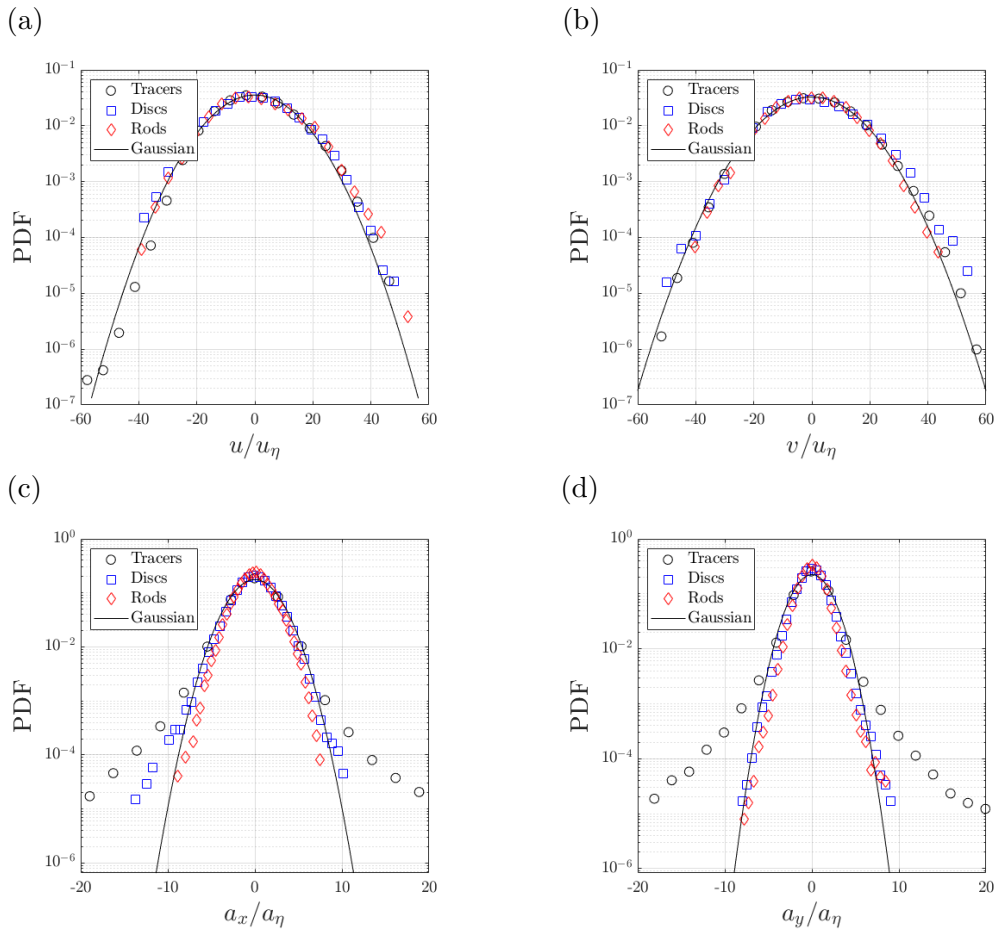

Figure 13: PDFs of the streamwise (a, c) and spanwise (b, d) velocity fluctuations (a, b) and accelerations (c, d) for the different particle types at the high flow rate. The distributions are normalized by Kolmogorov scaling. The continuous lines represent normalized Gaussian distributions.

The diffusion coefficient is then obtained by integrating the Lagrangian velocity autocorrelation which for long times t reaches a plateau due to the decay of the autocorrelation. As our autocorrelation functions are only physical for times just below $\tau = 1$ s we need to extrapolate the data to sufficiently long times. To do this, we use the second-order stochastic model proposed by Sawford (1991):

$$\rho^L(\tau) = \frac{T_L \mathrm{e}^{-t/T_L} - T_2 \mathrm{e}^{-t/T_2}}{T_L - T_2} \tag{28}$$

Here, two time scales are involved: the integral length scale T_L and a characteristic time scale related to the turbulent dissipation T_2. The former is related to the energy input and is defined as the characteristic decay time of the Lagrangian velocity autocorrelation function which is equivalent to:

$$T_L = \int_0^\infty \rho_U^L(\tau) d\tau \tag{29}$$

It is estimated by least-square fitting ρ_U^L to a function Ae^{-t/T_L} up to time delays of 0.8 s and 0.6 s for the low and high flow rates, respectively, at which point the autocorrelation has decayed to approximately 0.5. The value of T_2 is a characteristic time scale related to ϵ. It is estimated by fitting the experimental data to Equation 28 and found to be approximately $0.3\tau_\eta$ (of the same order as in 3D turbulence studies, e.g. Mordant et al. (2004) and Voth et al. (2002)). The diffusion coefficient is finally determined by the asymptotic behaviour of K (Equation 21) for long times and is plotted in Figure 15 for the different particle types and for both considered flow rates. We clearly see an increase in diffusivity with increasing Re, which is expected as turbulent flows enhance mixing processes; and, importantly, that the larger particles have larger diffusion coefficients than the smaller tracer particles, with the discs dispersing faster than the rods.

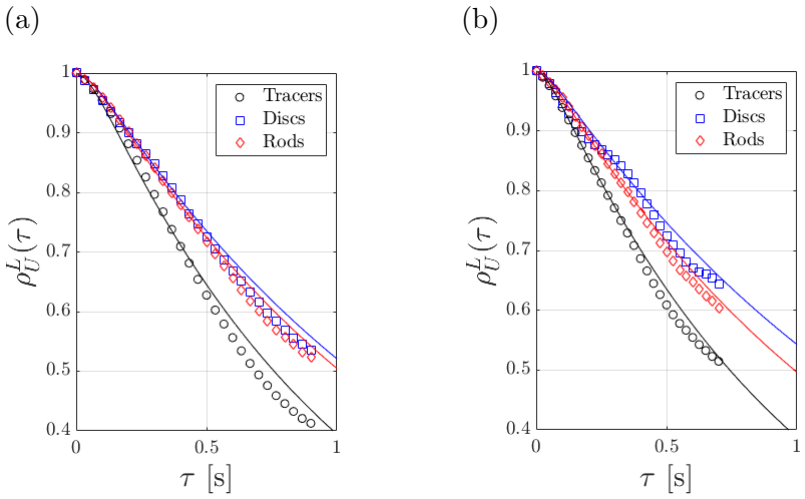

Figure 14: The Lagrangian velocity autocorrelation function of each particle type for (a) low and (b) high flow rates. The solid lines are the autocorrelation functions computed using Equation 28 which are integrated to obtain diffusion coefficients.

To verify this notion, we consider the MSD of the particles due to turbulent fluctuations. We define the MSD due to turbulent fluctuations as:

$$\langle X(t)^2 \rangle = \langle (\mathbf{x}(t) - \mathbf{x}(t_0) - \langle \mathbf{u} \rangle \Delta t)^2 \rangle \tag{30}$$

where $\langle \mathbf{u} \rangle \Delta t$ is the advective displacement due to the global mean flow during the time interval $t - t_0$. Unlike Equation 23, the last term in the above is subtracted to isolate the contribution of the turbulent fluctuations. The advective flow is taken to be a spatially uniform motion, leveraging the high spatial homogeneity in the considered sub-region; this avoids the ambiguities associated to subtracting different advective displacements at different points along the same trajectory. The MSD of each particle type for both flow rates

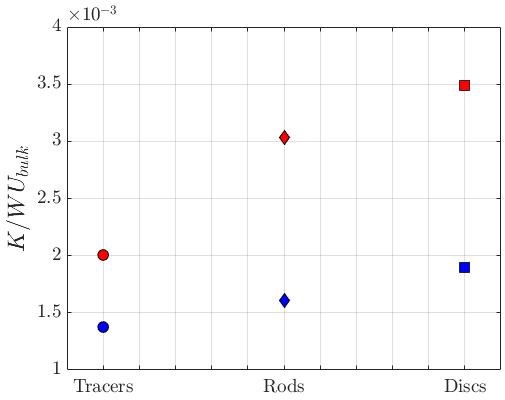

Figure 15: Normalized diffusivity of the different particle type for both the low (blue) and high (red) flow rates.

is plotted in Figure 16. This corroborates the finding that, in both the high and low flow rates considered here, the discs spread faster than the rods which spread faster than the tracers.

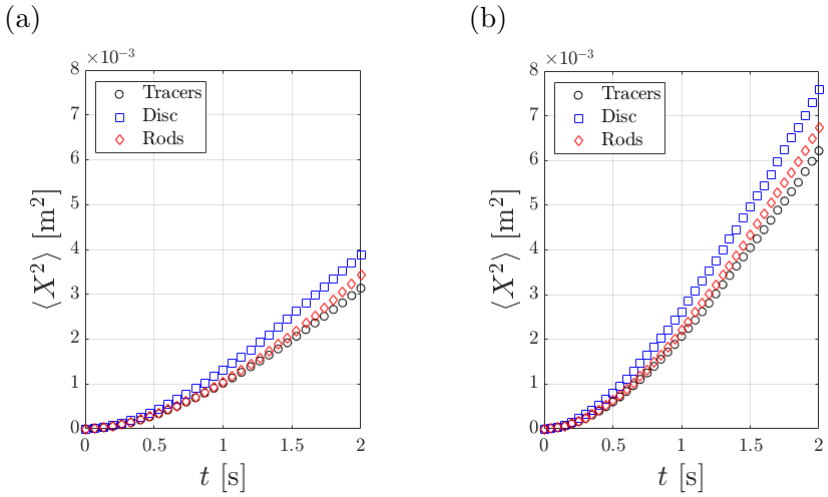

Figure 16: The MSD due to turbulent velocity fluctuations of each particle type for (a) low and (b) high flow rates.

We finally turn to pair-dispersion, investigating how fast particle pairs separate from each other. Here we calculate the MSS (Equation 24) after subtracting the initial separation D_0 to account for possible correlation between initial separation and relative velocity of the pair (Ouellette et al., 2006b). Figure 17 shows the MSS of each particle type for both flow rates. The t^2 scaling predicted by Batchelor (1950) for relatively short times is recovered, which indicates that the recorded trajectories are in the so-called ballistic regime. This is also evident in Figure 16 as the MSD also scales with t^2 for times $t \ll T_L$ which is expected in this regime (Taylor, 1921). Again, the discs are seen to separate faster than the rods (although this is evident only at the higher flow rate), and the latter separate faster than the tracers.

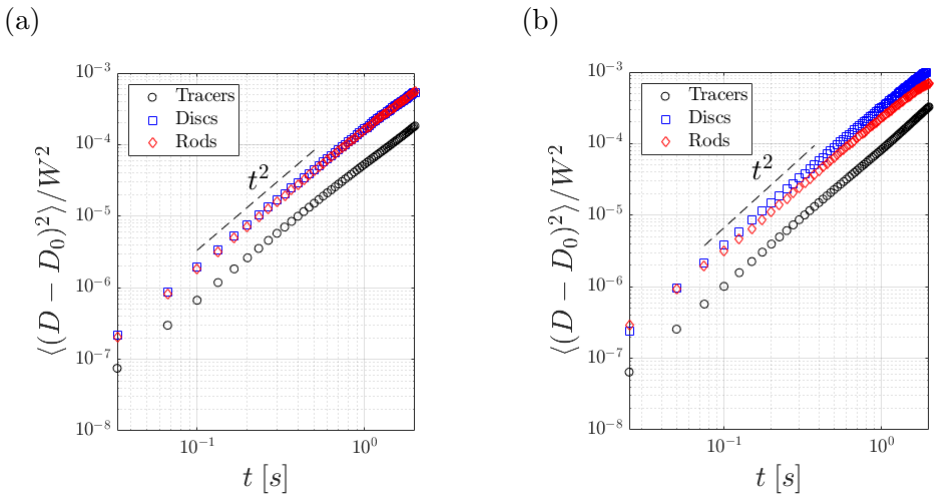

Figure 17: The MSS of each particle type for (a) low and (b) high flow rates. The dashed line corresponds to t^2 (ballistic) scaling.

4.3 Rod Orientation

Inertial anisotropic particles in turbulence move according to their inertia and rotate due to the hydrodynamic forces and torques they experience (Voth & Soldati, 2017). Therefore, it is of interest to investigate the rods orientation in the considered sub-region. Specifically, how the rods orient themselves and rotate on the turbulent free surface. Simulations of inertial fibres in 3D turbulent channel flows have found that in the near-wall region, where local velocity gradients (shear stress') are large, fibres preferentially align themselves with the flow direction. This degree of alignment with the flow direction becomes weaker moving away from the wall region and eventually vanishes at the core region, where local velocity gradients are small, and turbulence is nearly homogeneous and isotropic (Njobuenwu & Fairweather, 2016). Therefore, having deduced homogeneity and isotropy within the sub-region of our flow, and the fact that the particle statistics are consistent with the classic phenomenology of homogeneous 3D turbulence, we would expect that the rods remain randomly oriented within the sub-region.

To consider the rods orientation we define $\hat{\mathbf{p}}$, the unit vector along the rod's semi-major axis. Figure 18a shows the PDF of the cosine of the angle between the streamwise direction $\hat{\mathbf{e}}_\mathbf{s}$ (in the appropriate curvilinear coordinate system) and $\hat{\mathbf{p}}$. In our experiments we find that the rods have a tendency to preferentially align themselves in the streamwise direction which differs from what is expected in 3D turbulence. Additionally, from the orientation correlation function (Figure 18b), we find that the rods rotate very slowly. The time scale associated with such rotation is not only significantly larger than τ_η but also much longer than T_L which indicates that the orientation dynamics, in this case, are not governed by the free surface turbulence. A point not fully investigated here. However, possible rational for this behaviour could include:

I. There are streamwise-elongated structures in the flow, which the rods align with, similarly to how they align themselves with near-wall structures in wall bounded tur-

bulence. These coherent structures would emerge from the subsurface flow and reach the free surface as the water level is relatively shallow. These structures could be not only due to the generic boundary layer, but also due to the complex topography of the OSL.

II. The rods feel significant drag due to their relatively large size, thus they align themselves in the streamwise direction to reduce that.

III. The rods, being inertial, are still responding to the effects of some strong shear they experienced upstream of the meander that is not visible in our FOV.

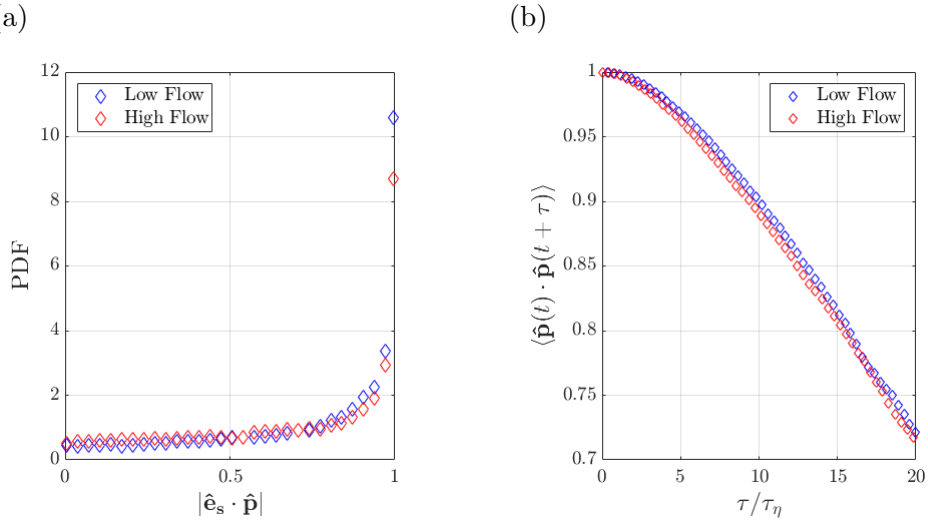

Figure 18: (a) PDF of the absolute value of the cosine of the angle between the streamwise direction and the unit vector along the rods semi-major axis. (b) Correlation function of the rods orientation.

We examining the Eulerian 2D divergence field of the tracers for both flow rates to identify if any streamwise-elongated structures appear in the FOV. The 2D divergence is defined as:

$$\nabla_H \cdot \mathbf{u} = \frac{\partial u}{\partial x} + \frac{\partial v}{\partial y} = -\frac{\partial w}{\partial z} \tag{31}$$

From Figure 19 we cannot clearly identify any visible emerging elongated structures. This does not necessarily rule out I. as there could be instantaneous structures that are lost through the temporal averaging process. In fact, upstream of the ROI is a riffle, an area with a fast current where rocks break the water surface, which could produce a jet-like structure responsible for this strong shear. Conducting similar experiments to those presented in this thesis, and imaging the rods over the riffle of the OSL we could investigate the Eulerian orientation field of the rods to address III.. If we observe that the rods are preferentially aligned in the streamwise direction before encountering the jet-like structure then we could conclude that this structure is not responsible for the rods alignment, leaving II. as a

plausible explanation for this behaviour. Nevertheless, we have determined that the rods are inertial and have finite-sized effects therefore it is plausible they may align themselves in the streamwise direction to reduce their drag. Nonetheless, these are mere speculations and further studies in canonical flow configurations are required to identify the logic behind this opposing behaviour.

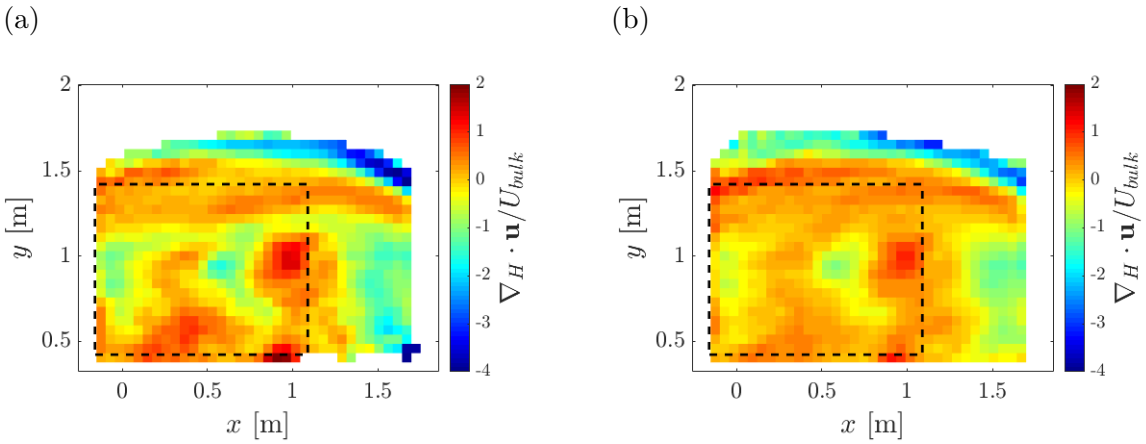

Figure 19: Two-dimensional divergence fields of the tracers for the (a) low and (b) high flow rates. The dashed box indicates the sub-region of the flow where approximate homogeneity and isotropy is observed.

Chapter 5

Conclusions

Motivated by the need of understanding the transport of plastic pollution in river flows, we have characterized the motion of particles of different shape and size floating on the surface of a field-scale turbulent stream using PTV. We have focused on a region of about 1.25 m^2 where the mean flow is relatively uniform and the RMS velocity fluctuations are approximately homogeneous and isotropic, which allows us to perform detailed statistical analysis of the particle motion in both the Eulerian and the Lagrangian perspectives. Millimetre-sized spherical particles, which are expected to follow the water flow fluctuations containing most of the turbulent kinetic energy, are used as tracers. The behaviour of their velocities, accelerations, velocity structure functions and velocity autocorrelations are consistent with the classic phenomenology of homogeneous 3D turbulence. This framework is then used to estimate, to first order accuracy, the spatial and temporal scales of the free surface turbulence.

From this analysis, the maximum dimension of the centimetre-sized discs and rods are found to be much larger than the Kolmogorov scales, η but much smaller than the integral scales of the turbulence, L_L. These larger particles are therefore expected to be inertial, i.e. to have a sizeable response time. One can thus anticipate that they will follow the energetic flow motions but filter out the small-scale turbulent fluctuations due this increased response time, and is commonly found for finite-size particles in 3D turbulence (Voth et al., 2002; Qureshi et al., 2007; Volk et al., 2011). We find that the larger floating particles in fact do have a modulated response to the small-scale fluctuations of the surface flow. This notion is shown by the single-point statistics, which indicate how the mean and fluctuating velocities of the larger particles are virtually indistinguishable from the tracers', but their acceleration variance is significantly smaller and its distribution less intermittent. The important consequence is that the larger particles disperse significantly faster on the free surface. Indeed, Lagrangian tracking indicates that their motion is more time-correlated compared to the tracers. This is interpreted to be a consequence of the ability of the larger discs and rods to filter out the small-scale, chaotic fluctuations of the turbulence. In terms of single-particle dispersion, the long-time-correlated motion of the discs and rods results in increased diffusion coefficients and faster-growing mean square displacements, according to the theory of Taylor (1921). The discs spread even faster than and rods, possibly due to the rotational dynamics of the latter, which may couple in non-trivial ways with their translational motion – a point not investigated here. The trend is also confirmed in terms of pair-dispersion, with mean square separations growing faster for the discs than for the rods, and both much faster than for the tracers.

The observed increase of turbulent diffusivity with particle inertia is consistent with classic results in 3D turbulence, at least when gravitational settling is negligible or absent (Squires & Eaton, 1991; Sabban & van Hout, 2011). Laboratory studies investigating the transport of inertial particles floating on free surface turbulence are lacking. As mentioned in the Introduction, Xia et al. (2019) found that the diffusivity of discs floating on wave-driven 2D turbulence decreased with increasing disc diameter. On the other hand, Ouellette

et al. (2008) had found the opposing trend for spheres located between the two layers of an electromagnetically forced 2D turbulence apparatus. In addition Yang et al. (2019) found that ellipsoids floating on wave driven 2D turbulence diffuse faster in the direction of their major axis if this is larger than the forcing scale. However, it is important to stress that 2D turbulence exhibits very different features compared to both 3D and free surface turbulence, notably in fundamental aspects such as the energy cascade and the intermittency of the velocity increments (Tabeling, 2000; Boffetta & Ecke, 2012; Xia et al. 2013; Rivera & Ecke, 2016). From the present study, instead, we observe that the 3D turbulence phenomenology applies both to the statistics of free surface turbulent flow and to the motion of inertial particles floating on it. This may have important implications for the modelling of floating particle transport. However, further investigation is required regarding the rotation of floating anisotropic particles. Well-controlled laboratory experiments are warranted to verify the generality of these observations. One could devise an experiment to study the transport of particles of different shape and size in a finite channel where turbulence at the free surface is generated using a static (or active) grid. In addition, characteristic features of shallow flows, such as transitional macro-vortices, have been found to greatly affect the single-particle and particle-pair dispersion (Stocchino et al., 2011); thus, systematic investigations of the effect of flow depth on the transport of finite-size particles are also warranted.

The present findings may have important consequences for the transport of plastics floating in river flows, as it provides insight on how finite-size particles spread as compared to smaller ones (and to fluid elements). Our experiments have been carried out in a relatively small stream; conceptually similar studies in larger rivers are recommended to confirm and generalize these results. In such cases, particle imaging would more challenging, and may require the use of unmanned aerial vehicles, which have recently been utilized to characterize natural stream flows (Blois et al., 2016; Liu et al., 2021). Future works shall also expand the parameter space in terms of particle shape and size, as well as material properties such as flexibility, considering that flexible particles may undergo large deformations in turbulent waters (Brouzet et al., 2014). Finally, while we have considered the case in which the free surface displayed negligible disturbances, waves are a key element in high Froude number flows and/or in the presence of wind shear. Indeed, recent theoretical and experimental studies indicate that waves profoundly impact the settling velocity of negatively buoyant particles, depending on their inertia and shape (DiBenedetto et al., 2017; Clark et al. 2020). Further studies of floating particles of different shape and size in wavy turbulent flows are thus in order.

REFERENCES

Baker, L. J., & Coletti, F. (2020). Particle-fluid-wall interaction of inertial spherical particles in a turbulent boundary layer. *Journal of Fluid Mechanics*, 908.

Bandi, M. M., Cressman, J. R., & Goldburg, W. I. (2007). Test of the fluctuation relation in Lagrangian turbulence on a free surface. *Journal of Statistical Physics*, 130(1), 27-38.

Barboza, L. G. A., Dick Vethaak, A., Lavorante B. R.B. O., Lundebye, A.-K., & Guilhermino, L. (2018). Marine microplastic debris: An emerging issue for food security, food safety and human health. *Marine Pollution Bulletin*, 113, 336-348.

Batchelor, G. K. (1950). The Application of the Similarity Theory of Turbulence to Atmospheric Diffusion. *Quarterly Journal of the Royal Meteorological Society*, 76(328), 133–46.

Berk, T., & Coletti, F. (2021). Dynamics of small heavy particles in homogeneous turbulence: A Lagrangian experimental study. *Journal of Fluid Mechanics*, 917.

Blois, G., Best, J.L., Christensen, K.T., Cichella, V., Donahue, A., Hovakimyan, N., Kennedy, A., & Pakrasi, I. (2016). Assessing the use of UAV to quantify flow processes in rivers, *River Flow*.

Boffetta, G., & Ecke, R. E. (2012). Two-dimensional turbulence. *Annual Review of Fluid Mechanics*, 917.

Brocchini, M., & Peregrine, D. H. (2001). The dynamics of strong turbulence at the free surfaces. Part 1. Description. *Journal of Fluid Mechanics*, 449, 225-254.

Brouzet, C., Verhille, G., & Le Gal, P. (2014). Flexible fiber in a turbulent flow: A macroscopic polymer. *Physical Review Letters*, 112(7).

Brunner, K., Kukulka, T., Proskurowski, G., & Law, K. L. (2015). Passive buoyant tracers in the ocean surface boundary layer: 2. Observations and simulations of microplastic marine debris. *Journal of Geophysical Research: Oceans*, 120(11), 7559–7573.

Burattini, P., Lavoie, P., & Antonia, R. A. (2005). On the normalized turbulent energy dissipation rate. *Physics of Fluids*, 17(9), 098103.

Carter, D., Petersen, A., Amili, O., & Coletti, F. (2016). Generating and controlling homogeneous air turbulence using random jet arrays. *Experiments in Fluids*, 57(12).

Chickadel, C. C., Talke, S. A., Horner-Devine, A. R., & Jessup, A. T. (2011). Infrared based measurements of velocity, turbulent kinetic energy, and dissipation at the water surface in a tidal river. *IEEE Geoscience and Remote Sensing Letters*, 8(5), 849-85.

Clark, L. K., DiBenedetto, M. H., Ouellette, N. T., & Koseff, J. R. (2020). Settling of inertial nonspherical particles in wavy flow. *Physical Review Fluids*, 5(12).

Cressman, J. R., Davoudi, J., Goldburg W. I., & Schumacher, J. (2004). Eulerian and Lagrangian studies in surface flow turbulence. *New Journal of Physics*, 6, 53.

DiBenedetto, M. H., Ouellette, N. T., & Koseff, J. R. (2017). Transport of anisotropic particles under waves. *Journal of Fluid Mechanics*, 837, 320-240.

Fiabane, L., Zimmermann, R., Volk, R., Pinton, J.-F., & Bourgoin, M. (2012). Clustering of finite-sized particles in turbulence. *Physical Review E*, 86(3).

Flores, O., Riley, J. J., & Horner-Devine, A. R. (2017). On the dynamics of turbulence near the free surface. *Journal of Fluid Mechanics*, 821, 248-265.

Guala, M., Liberzon, A., Tsinober, A., & Kinzelbach, W. (2007). An experimental investigation of Lagrangian correlation of small-scale turbulence at low Reynolds number. *Journal of Fluid Mechanics*, 574, 405-427.

Halden, R. U. (2010). Plastics and health risks. *Annual Review of Public Health*, 31(1), 179-194.

Herlina, H, & Wissink, J. G. (2014). Direct numerical simulation of turbulent scalar transport across a flat surface. *Journal of Fluid Mechanics*, 744, 217-249.

Hunt, J. C. R., & Graham, J. M. R. (1978). Free-stream turbulence near plane boundaries. *Journal of Fluid Mechanics*, 84(2), 209.

Isobe, A., Kubo K., Tamura, Y., Kako, S., Nakashima, E., & Fujii, N. (2014). Selective transport of microplastics and mesoplastics by drifting in coastal waters. *Marine Pollution Bulletin*, 89(1-2), 324-330.

Jin, T., & Liao, Q. (2019). Application of large-scale PIV in river surface turbulence measurements and water depth estimation. *Flow Measurement and Instrumentation*, 6, 142-152.

Jung, J., Yeo, Y., & Lee, C. (2008). Behavior of heavy particles in isotropic turbulence. *Physical Review E*, 77(1).

Kolmogorov, A. N. (1941). Local structure of turbulence in an incompressible viscous fluid at very large Reynolds numbers. *Proceedings of the USSR Academy of Sciences*, 30.

Kukulka, T., Proskurowski, G., Morét-Ferguson, S., Meyer, D. W., & Law, K. L. (2012). The effect of wind mixing on the vertical distribution of buoyant plastic debris. *Geophysical Research Letters*, 39(7).

Lebreton, L., Slat, B., Ferrari, F., Sainte-Rose, B., Aitken, J., Marthouse, R., Hajbane, S., Cunsolo, S., Schwarz, A., Levivier, A., Noble, K., Debeljak, P., Maral, H., Schoeneich-Argent, R., Brambini, R., & Reisser, J. (2018). Evidence that the Great Pacific Garbage Patch is rapidly accumulating plastic. *Scientific Reports*, 8(1).

Liu, W.-C., Lu, C.-H., Huang, W.-C. (2021). Large-scale particle image velocimetry to measure streamflow from videos recorded from unmanned aerial vehicle and fixed imaging system. *Remote Sensing*, 13(14), 2661.

Lovecchio, S., Marchioli, C., & Soldati, A. (2013). Time persistence of floating-particle clusters in free-surface turbulence. *Physical Review E*, 88(3).

Machicoane, N., & Volk, R. (2016). Lagrangian velocity and acceleration correlations of larger inertial particles in a closed turbulent flow. *Physics of Fluids*, 28(3), 035113.

Magnaudet, J. (2003). High-Reynolds-number turbulence in a shear-free boundary layer: revisiting the Hunt-Graham theory. *Journal of Fluid Mechanics*, 484, 167–196.

McKenna, S. P., & McGillis, W. R. (2004). The role of free-surface turbulence and surfactants in air-water gas transfer. *International journal of Heat and Mass Transfer*, 47(3), 539-553.

Meijer, L. J. J., van Emmerik, T., van der Ent, R., Schmidt, C. & Lebreton, L. (2021). More than 1000 rivers account for 80% of global riverine plastic emissions into the ocean. *Science Advances*, 7(18).

Mendez, M. A., Raiola, M., Masullo, A., Discetti, S., Ianiro, A., Theunissen, R., & Buchlin, J.-M. (2017). POD-based background removal for particle image velocimetry. *Experimental Thermal and Fluid Science*, 80, 181-192.

Mordant, N., Lévêque, E., & Pinton, J.-F. (2004). Experimental and numerical study of the Lagrangian dynamics of high Reynolds turbulence. *New Journal of Physics*, 6, 116.

Nemes, A., Dasari, T., Guala, M., & Coletti, F. (2017). Snowflakes in the atmospheric surface layer: observation of particle-turbulence dynamics. *Journal of Fluid Mechanics*, 814, 592-613.

Nikora, V., Nokes, R., Veale, W., Davidson, M., & Jirka, G. H. (2007). Large-scale turbulent structure of uniform shallow free-surface flows. *Environmental Fluid Mechanics*, 7(2), 159-172.

Njobuenwu, D. O., & Fairweather, M. (2016). Simulation of inertial fibre orientation in turbulent flow. *Physics of Fluids*, 28(6), 063307.

Ouellette, N. T., O'Malley, P. J. J., & Gollub, J. P. (2008) Transport of finite-sized particle in chaotic flow. *Physical Review Letter*, 101(17).

Ouellette, N. T., Xu H., Bourgoin, M., & Bodenschatz, E. (2006a). Small-scale anisotropy in Lagrangian turbulence. *New Journal of Physics*, 8(6), 102.

Ouellette, N. T., Xu H., Bourgoin, M., & Bodenschatz, E. (2006b). An experimental study of turbulent relative dispersion models. *New Journal of Physics*, 8(6), 109.

Parsa, S., Guasto, J. S., Kishore, M., Oullette, N. T., Gollub, J. P., & Voth, G. A. (2011). Rotation and alignment of rods in two-dimensional chaotic flow. *Physics of Fluids*, 23(4), 043302.

Parsheh, M., Sotiropoulos F., & Porté-Agel, F. (2010). Estimation of power spectra of acoustic-doppler velocimetry data contaminated with intermittent spikes. *Journal of Hydraulic Engineering*, 136(6), 368-378.

Pope, S. B. (2001). Turbulent flows. *Measurement Science and Technology*, 112(11).

Qureshi, N. M., Bourgoin, M., Baudet, C., Cartellier, A., & Gagne, Y. (2007). Turbulent transport of material particles: An experimental study of finite size effects. *Physical Review Letters*, 99(18).

Richardson, L. F. (1926). Atmospheric diffusion shown on a distance-neighbour graph. *Proceedings of the Royal Society of London A*, 110(756), 709-737.

Rivera, M. K., & Ecke R. E. (2016). Lagrangian statistics in weakly forced two-dimensional turbulence. *Chaos: An Interdisciplinary Journal of Nonlinear Science*, 26(1), 012103.

Sabban, L., & van Hout, R. (2011). Measurements of pollen grain dispersal in still air and stationary, near homogeneous, isotropic turbulence. *Journal of Aerosol Science*, 42(12), 867–82.

Saddoughi, S. G., & Veeravalli, S. V. (1994). Local isotropy in turbulent boundary layers at high Reynolds number. *Journal of Fluid Mechanics*, 268, 333-372.

Sawford, B. L. (1991). Reynolds number effect in Lagrangian stochastic models of turbulent dispersion. *Physics of Fluids A: Fluid Dynamics*, 3(6), 1577-1586.

Sawford, B. L. (2001). Turbulent relative dispersion. *Annual Review of Fluid Mechanics*, 33(1), 289-317.

Shen, L., & Yue, D. K. P. (2001). Large-eddy simulation of free-surface turbulence. *Journal of Fluid Mechanics*, 440, 75-116.

Shen, L., Zhang, X., Yue, D. K. P., & Triantafyllou, G. S. (1999). The surface layer for free-surface turbulent flows. *Journal of Fluid Mechanics*, 386, 167-212.

Squires, K. D., & Eaton J. K. (1991). Measurements of particle dispersion obtained from direct numerical simulations of isotropic turbulence. *Journal of Fluid Mechanics*, 226, 1-35.

Sreenivasan, K. R., & Antonia, R. A. (1997). The phenomenology of small-scale turbulence. *Annual Review of Fluid Mechanics*, 226, 1-35.

Stocchino, A., Besio, G., Angiolani, S., & Brocchini, M. (2011). Lagrangian mixing in straight compound channels. *Journal of Fluid Mechanics*, 675, 168-198.

Tabeling, P. (2002). Two-dimensional turbulence: A physicist approach. *Physics Reports*, 362(1), 1-62.

Tauro, F., Petroselli, A., Porfiri, M., Giandomenico, L., Bernardi, G., Mele, F., Spina, D., & Grimaldi, S. (2016). A novel permanent gauge-cam station for surface-flow observations on the Tiber River. *Geoscientific Instrumentation, Methods and Data Systems*, 5(1), 241-251.

Tauro, F., Piscopia, R., & Grimaldi, S. (2019). PTV-Stream: A simplified particle tracking velocimetry framework for stream surface flow monitoring. *CATENA*, 172, 378-386.

Taylor, G. I. (1921). Diffusion by continuous movements. *Proceedings of the London Mathematical Society*, 20(1), 196-212.

Tennekes, H., & Lumley, J. A first course in turbulence. *The MIT Press*, 1st Edition, 1972.

Toschi, F., & Bodenschatz, E. (2009). Lagrangian properties of particles in turbulence. *Annual Review of Fluid Mechanics*, 41(1), 375-404.

Turney, D. E., & Banerjee, S. (2013). Air-water gas transfer and near-surface motions. *Journal of Fluid Mechanics*, 733, 588-624.

van Emmerik, T. & Schwarz, A. (2019). Plastic debris in rivers. *WIREs Water*, 7(1).

Volk, R., Calzavarioni, E., Lévêque, E., & Pinton, J.-F. (2011). Dynamics of inertial particles in a turbulent von Karman flow. *Journal of Fluid Mechanics*, 668, 223-235.

Voth, G. A., La Porta, A., Crawford, A. M., Alexander, J., & Bodenschatz, E. (2002). Measurement of particle accelerations in fully developed turbulence. *Journal of Fluid Mechanics*, 469, 121-160.

Voth, G. A., & Soldati, A. (2017). Anisotropic particles in turbulence. *Annual Review of Fluid Mechanics*, 49(1), 249-276.

Xia, H., François, N., Punzmann, H., & Shats, M., (2013). Lagrangian scale of particle dispersion in turbulence. *Nature Communications*, 4(1).

Xia, H., François, N., & Shats, M., (2019). Tunable diffusion in wave-driven two-dimensional turbulence. *Journal of Fluid Mechanics*, 865, 811-830.

Yang, J., François, N., Punzmann, H., Shats, M., & Xia, H. (2019). Diffusion of ellipsoids in a laboratory two-dimensional turbulent flow. *Physics of Fluids*, 31(8), 085116.